crystals

MDPI

Article

Research on the Influence of Different Aging Temperatures on the Microstructure and Properties of GH2787 Alloy

Yan Wang [1,2,3], Guohua Xu [4], Shengkai Gong [1], Shusuo Li [1], Juan Deng [1,2], Tianyi Wang [4], Zhen Liu [4,*] and Wenqi Guo [1,5,*]

[1] Research Institute of Aero-Engine, Beihang University, Beijing 100191, China
[2] AECC Chengdu Engine Co., Ltd., Chengdu 610503, China
[3] Taihang Laboratory, Chengdu 610213, China
[4] Gaona Aero Material Co., Ltd., Beijing 100081, China; a4035333@hotmail.com (T.W.)
[5] Suzhou Laboratory, No. 388, Ruoshui Street, SIP, Suzhou 215123, China
* Correspondence: liuz_ustb@163.com (Z.L.); guowenqi@buaa.edu.cn (W.G.)

Abstract

This study systematically investigates the microstructural evolution and mechanical properties of GH2787 superalloy following solution treatment at 1140 °C and subsequent aging within the temperature range of 770 °C to 920 °C. The results indicate that aging at 770 °C and 820 °C promotes the precipitation of a high density of finely dispersed γ' precipitates with minimal interparticle spacing. In contrast, a significant coarsening of the γ' particles, accompanied by a sparse distribution and a notable increase in interparticle spacing, was observed at the higher aging temperatures of 870 °C and 920 °C. Mechanical characterization reveals that the ultimate tensile strength (UTS) and yield strength (YS) experienced a moderate decrease as the aging temperature increased from 770 °C to 820 °C, followed by a pronounced drop at 870 °C and 920 °C. Conversely, the impact toughness exhibited a non-monotonic trend: it gradually decreased, reaching a minimum at 820 °C, before rapidly increasing with further rises in aging temperature. Quantitative analysis of the strengthening contributions demonstrates that solid-solution and precipitation strengthening are the dominant mechanisms. The marked decline in yield strength at elevated aging temperatures is primarily attributed to the diminished precipitation strengthening effect due to γ' coarsening. Furthermore, the variation in impact toughness can be linked to the proportion and size of dimples observed on the fracture surfaces, indicating a transition in the fracture mechanism driven by microstructural evolution.

Keywords: GH2787 superalloy; gamma prime (γ') precipitates; dislocations; aging temperature; tensile strength

Check for updates

Academic Editor: Shouxun Ji

Received: 29 November 2025
Revised: 15 January 2026
Accepted: 20 January 2026
Published: 23 January 2026

Correction Statement: This article has been republished with a minor change. The change does not affect the scientific content of the article and further details are available within the backmatter of the website version of this article.

Copyright: © 2026 by the authors. Licensee MDPI, Basel, Switzerland. This article is an open access article distributed under the terms and conditions of the Creative Commons Attribution (CC BY) license.

1. Introduction

Aero-engines and spacecraft propulsion systems, serving as the core power units in the aerospace field, fundamentally determine the overall performance, reliability, and economic viability of the vehicle. The high-temperature components within these systems, such as combustion chambers, guide vanes, and turbine disks, are consistently subjected to extreme service conditions characterized by elevated temperatures and high pressures. Consequently, the materials employed in these components must meet exceptionally stringent performance requirements [1–5]. The GH2787 superalloy has emerged as a prime

candidate material for manufacturing critical parts, including combustion chambers, compressor blades, and turbine disks, owing to its superior high-temperature strength, excellent oxidation resistance, and remarkable corrosion resistance [6].

The strengthening mechanisms of the GH2787 alloy primarily involve solid-solution strengthening contributed by elements such as Cr and W, coupled with precipitation strengthening from the finely dispersed γ'-Ni_3 (Al, Ti) precipitates that form during the aging process. Furthermore, the addition of trace elements like B and Ce enhances performance by purifying and strengthening grain boundaries. This alloy exhibits an outstanding balance of high strength and ductility within the temperature range of 500–700 °C, complemented by good fatigue resistance and corrosion resistance. Its maximum service temperature can reach up to 800 °C. Currently, the GH2787 alloy is extensively utilized domestically and internationally for critical aero-engine components such as working blades and turbine disks, successfully fulfilling the demands of these severe operating environments.

The GH2787 alloy is a typical precipitation-strengthened superalloy, for which the conventional heat treatment primarily consists of two stages: solution treatment and aging treatment. The solution treatment is designed to fully dissolve the precipitates into the matrix, thereby forming a homogeneous supersaturated solid solution. Subsequently, the aging treatment is employed to promote the uniform precipitation of the strengthening γ' phase, which enhances the overall strength-toughness balance of the alloy [7]. Variations in the aging temperature significantly alter the size, morphology, and distribution of these precipitates, consequently influencing the plastic deformation mechanisms of the alloy. During tensile deformation, the dominant interaction mechanism between dislocations and precipitates transitions from "shearing" to "bypassing (Orowan looping)" as the aging condition changes. This transition in mechanisms plays a critical role in the synergistic regulation of the alloy's strength and ductility [8,9].

Research conducted by Liu et al. demonstrated that appropriately reducing the solution temperature contributes to refining the grain size and improving its uniformity in GH2787 alloy, thereby enhancing its comprehensive mechanical properties [10]. In a separate study, X H Li et al. [11] systematically investigated the forging process of GH2787 alloy blades. They highlighted that, in addition to heat treatment parameters, the grain size and distribution developed during the forging deformation play a critical role in determining the homogeneity of the final microstructure. This as-forged structure provides an essential microstructural foundation for subsequent grain size control during heat treatment.

Given the decisive role of heat treatment in determining the microstructure and mechanical properties of superalloys, it inevitably exerts a profound influence on their in-service performance and long-term microstructural stability. However, systematic studies on the influence of aging temperature on the microstructural evolution and corresponding property mechanisms in GH2787 alloy remain relatively scarce. Therefore, this work aims to systematically investigate the microstructural evolution of GH2787 alloy under different aging temperatures and its impact on mechanical properties, thereby providing a theoretical foundation for optimizing the heat treatment processes of this alloy.

2. Experimental Details

The nominal chemical composition of the GH2787 alloy employed in this study is: Fe-0.054C-15.13Cr-35.54Ni-1.22Al-2.81Ti-3.22W-0.082Si-0.015Mn-0.010B (wt.%). The master ingot was first forged into a billet and then processed into rods with a diameter of 30 mm. Specimens for systematic heat treatment investigation were subsequently sectioned from these rods. Figure 1 presents the equilibrium phase diagram of the GH2787 alloy. Thermodynamic analysis indicates that within the temperature range of 600–928 °C, the

mass fraction of the γ′ phase decreases gradually from approximately 18% with increasing temperature, until it completely dissolves into the matrix at 928 °C. In contrast, the content of TiC carbides remains relatively stable at about 0.3% over a wide temperature range and only dissolves back into the matrix at 1336 °C.

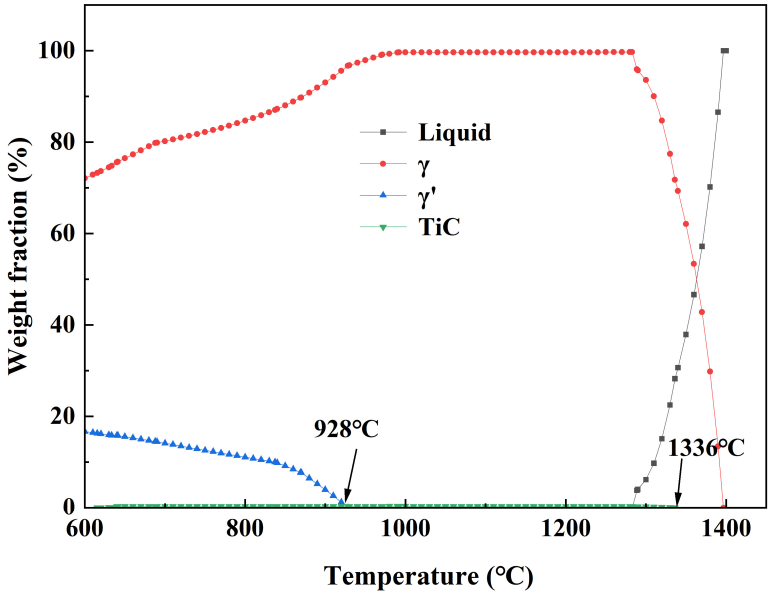


Figure 1. The equilibrium phase diagram of GH2787 alloy.

The heat treatment regimen applied in this work consisted of a primary solution treatment at 1140 °C for 4 h, followed by aging treatments at 770 °C, 820 °C, 870 °C, and 920 °C, respectively, each held for 16 h. The specimens subjected to these different aging conditions were then characterized by tensile tests, impact toughness tests, and systematic microstructural analysis.

In this study, the axial tensile specimens were machined into cylindrical specimens with a gauge diameter of 5 mm and M10 threaded ends, in accordance with the relevant standard. The impact tests utilized standard Charpy U-notch specimens with dimensions of 10 mm × 10 mm × 55 mm. All mechanical tests were conducted at room temperature. To ensure data reliability, three replicate specimens were prepared for each heat treatment condition, and the average value of the test results was reported as the final effective data.

The experimental procedure involved the standard preparation of metallographic specimens followed by microstructural characterization via optical microscopy. Quantitative analysis of grain size was performed on the captured micrographs using Nano Measure 1.2 software. To ensure statistical significance, measurements were conducted on no fewer than 500 grains per specimen, from which the mean grain size was derived. To reveal the γ′ precipitates, the polished specimens were electrochemically etched in a 10% aqueous oxalic acid solution at 3–6 V for 5–15 s. The microstructures were then observed using a scanning electron microscope (SEM), with more than 30 images captured for each specimen to ensure statistical significance. The size of the γ′ particles was quantitatively analyzed using Image-Pro Plus (IPP) software (version 6.0), with a minimum of 2000 particles measured per condition to obtain a reliable average value.

The fracture surfaces of impact specimens were examined using scanning electron microscopy (SEM). To ensure statistical relevance, the average dimple size was determined by measuring the dimensions of no fewer than 1000 dimples from representative areas. For transmission electron microscopy (TEM) observation, samples were first sectioned and mechanically pre-thinned to 30–50 μm, then punched into 3 mm disks. Final thinning

was performed by twin-jet electropolishing in a solution of 10% perchloric acid in ethanol (10% $HClO_4$ + 90% C_2H_5OH) at a temperature maintained between −20 and −30 °C, with an applied voltage of 20–35 V, until perforation occurred. The TEM was employed to observe dislocation configurations and other substructural features. Selected area electron diffraction (SAED) was used to identify the crystal structure of the γ' precipitates. Additionally, energy-dispersive X-ray spectroscopy (EDS) was utilized for microchemical analysis, while X-ray diffraction (XRD) was applied to determine phase composition and estimate dislocation density.

3. Results

3.1. Mechanical Properties

Figure 2 showed the influence of different aging temperatures on the strength and toughness of GH2787 alloy. As the aging temperature increased from 770 °C to 920 °C, both the tensile strength and yield strength of the GH2787 alloy bar exhibited a continuous decline. Specifically, the ultimate tensile strength decreased from 1125 ± 11 MPa at 770 °C to 878 ± 6 MPa at 920 °C, while the yield strength dropped from 715 ± 4 MPa to 433 ± 4 MPa over the same temperature range. In contrast, the impact toughness of the alloy followed a non-monotonic trend: the impact energy first decreased from 39 ± 3 J at 770 °C to a minimum of 14 ± 2 J at 810 °C, and then increased significantly to 60 ± 3 J as the temperature was further raised to 920 °C. Figure 2c,d presented the room-temperature tensile stress–strain curves and the corresponding elongation values, respectively, under different aging temperatures. As the aging temperature increased from 770 °C to 820 °C, the elongation decreased from 15.5 ± 0.8% to 7.5 ± 1.0%. With a further rise in temperature to 920 °C, the elongation increased again, reaching 29.5 ± 0.9%.

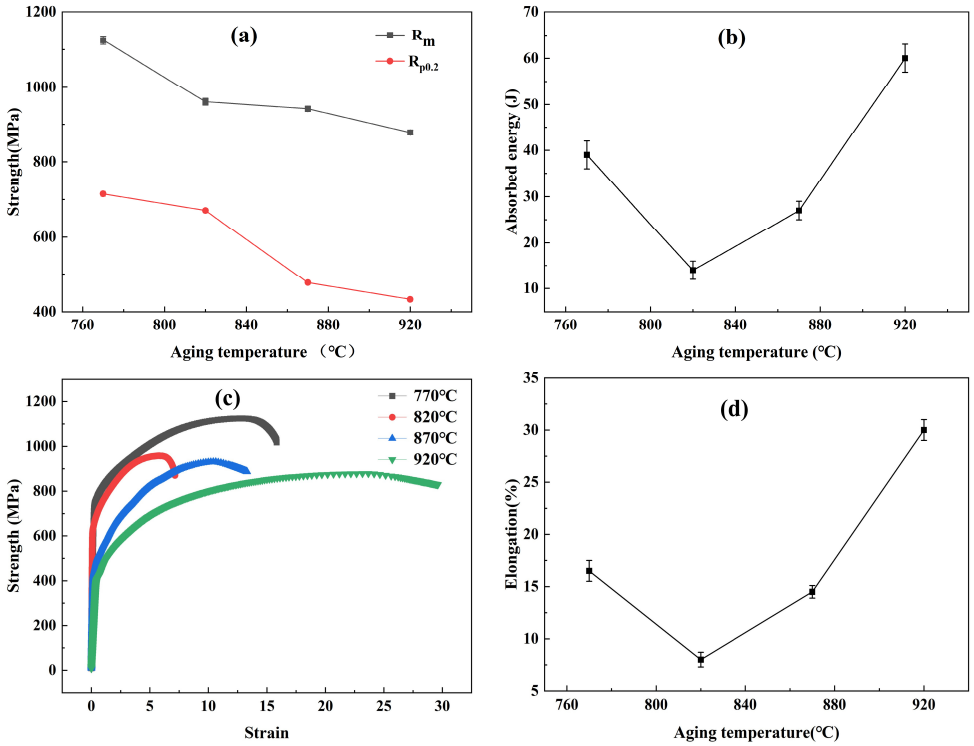


Figure 2. The influence of different aging temperatures on the mechanical properties of GH2787 alloy: (**a**) strength, (**b**) toughness, (**c**) stress–strain curve, and (**d**) elongation.

3.2. Microstructure

3.2.1. Prior Austenite Grain

Figure 3 displays the grain morphology of the GH2787 alloy subjected to different aging temperatures. Statistical analysis reveals that as the aging temperature increases from 770 °C to 890 °C, the corresponding average grain sizes are measured as 294.6 ± 8.3 μm, 285.8 ± 12.1 μm, 313.2 ± 10.4 μm, and 298.1 ± 9.7 μm, respectively. These results indicate that varying the aging temperature within this range has a negligible influence on the final grain size. As can be inferred from the equilibrium phase diagram in Figure 1, the dissolution temperature of the γ′ phase in GH2787 alloy is approximately 928 °C. Since all the employed aging temperatures are below this critical value, the γ′ precipitates remain stable and exert a strong pinning force on the grain boundaries, effectively inhibiting their migration. This pinning effect is the primary reason for the observed stability in grain size across the different aging conditions.

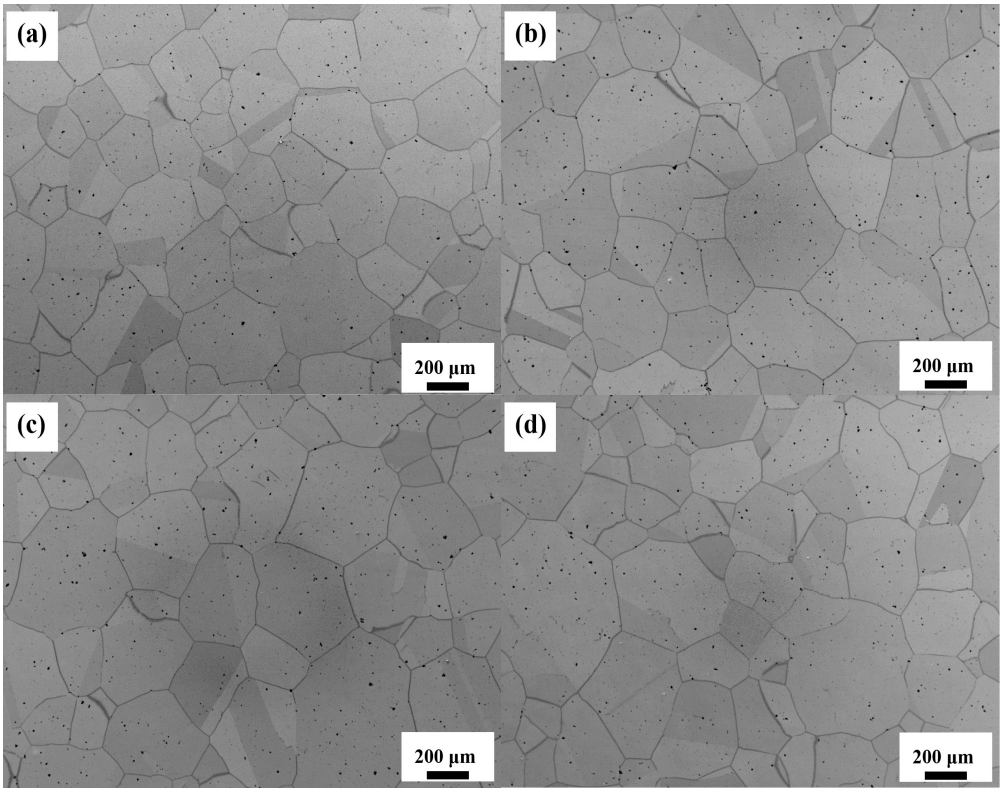


Figure 3. Grain morphology of GH2787 alloy at different aging temperatures: (**a**) 770 °C, (**b**) 820 °C, (**c**) 870 °C, (**d**) 920 °C.

3.2.2. Precipitates

Figure 4 presents the morphology and corresponding size distribution of γ′ precipitates in the GH2787 alloy under different aging temperatures. The results clearly indicate that the aging temperature exerts a remarkable influence on the size, spatial distribution, and number density of the γ′ phase. As shown in Figure 4a–d, the statistical size distributions of the γ′ particles under each condition, provided in the upper-right insets, are found to closely follow a normal distribution. A systematic quantitative analysis of the γ′ precipitate size, distribution characteristics, and number density under various aging conditions was further conducted using the Nano Measurer software (version 1.2).

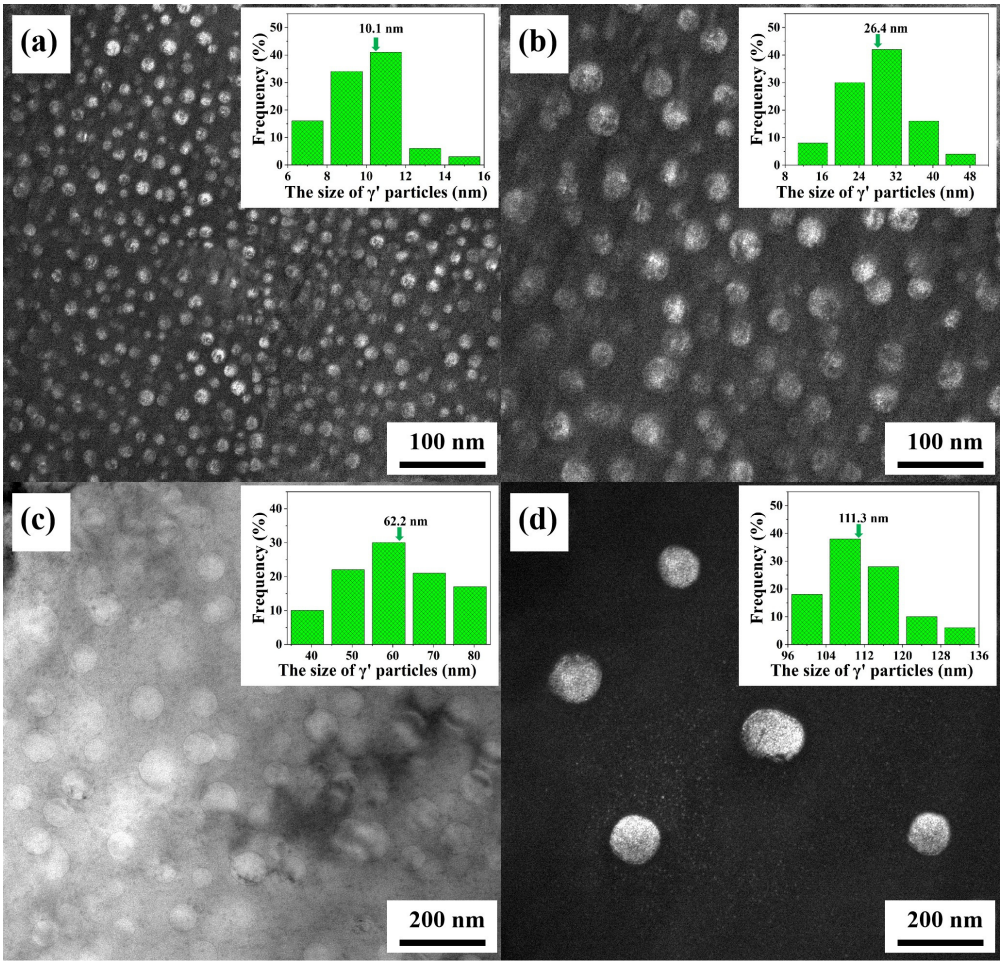


Figure 4. Morphology of γ′ particles of GH2787 alloy at different aging temperatures: (**a**) 770 °C, (**b**) 820 °C, (**c**) 870 °C, (**d**) 920 °C.

Figure 5 summarizes the statistical results of the average size, interparticle spacing, and number density of γ′ precipitates in the GH2787 alloy after solution treatment at 1140 °C and subsequent aging at 770 °C, 820 °C, 870 °C, and 920 °C. As shown in Figure 5a, the average diameter of the γ′ particles increased markedly from 10.1 ± 2.2 nm at 770 °C to 111.4 ± 9.2 nm at 920 °C. Correspondingly, the number density of the γ′ precipitates (Figure 5b) decreased dramatically from 98.2 ± 6.6 × 10^{13} m^{-2} at 770 °C to only 0.4 ± 0.1 × 10^{13} m^{-2} at 920 °C. It is worth noting that the average interparticle spacing (Figure 5c) exhibited a gradual increase from 18.6 ± 3.5 nm to 74.9 ± 11.8 nm as the aging temperature rose from 770 °C to 870 °C. However, a rapid coarsening occurred at 920 °C, leading to a significant jump in the interparticle spacing to 226.2 ± 24.4 nm.

These phenomena can be attributed to differences in atomic diffusion behavior and phase equilibrium at various temperatures. During aging at a relatively low temperature of 770 °C, the limited atomic diffusion rate, combined with a high equilibrium volume fraction of the γ′ phase, results in a sluggish Ostwald ripening process [12,13]. Consequently, the resulting γ′ microstructure exhibits a fine-scale and densely distributed metastable characteristic. As the aging temperature increases to 870 °C and above, atomic mobility is significantly enhanced, while the equilibrium fraction of the γ′ phase decreases. To reduce the total interfacial energy and approach the thermodynamic equilibrium state at these elevated temperatures, the Ostwald ripening process is markedly accelerated. After 20 h of aging, the γ′ particles undergo pronounced coarsening, leading to an increased

average size, a reduced number density, and a microstructure that evolves toward a more stable state.

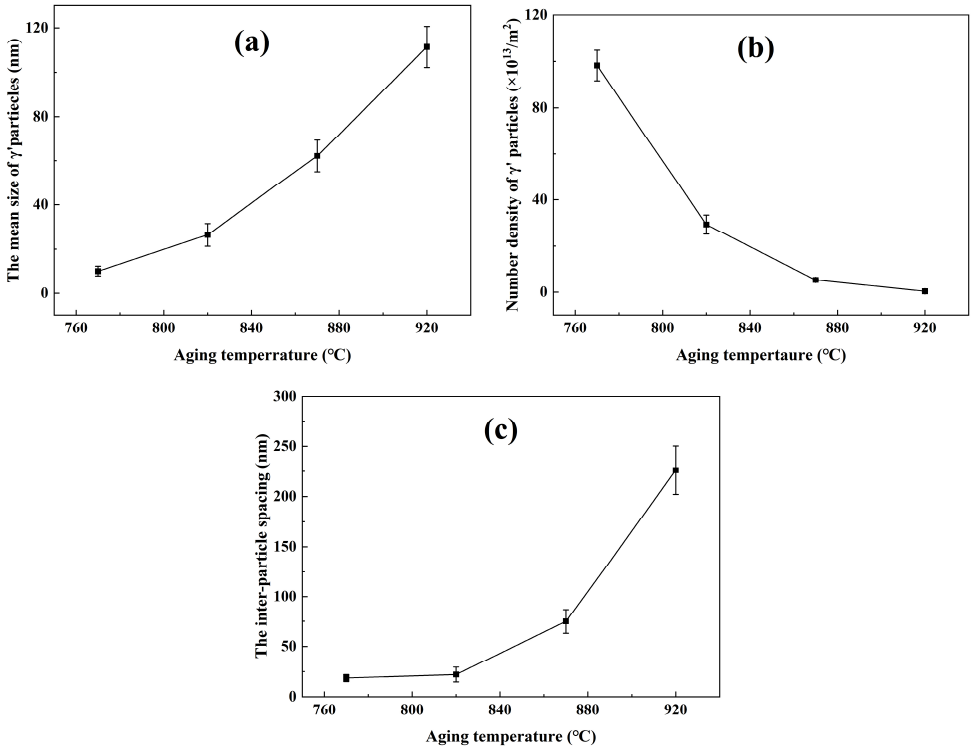


Figure 5. Statistical information of γ' particles at different aging temperatures: (**a**) average size, (**b**) quantity density, (**c**) particle spacing.

Figure 6 presents TEM characterization results of the precipitates in the GH2787 alloy. In addition to the uniformly dispersed γ' strengthening phase shown in Figure 4, a small number of coarse precipitate particles were observed along grain boundaries. Systematic examination of multiple fields of view confirmed the absence of such particles within grain interiors. Based on the diffraction pattern analysis shown in Figure 6b, these precipitates were identified as TiC carbides, which is composed predominantly of carbon (C) and titanium (Ti), with minor amounts of tungsten (W). The TiC particles exhibited an average size of approximately 150–400 nm, an interparticle spacing of 6–8 μm, and an extremely low number density of about $(1.4 \pm 0.3) \times 10^7$ m^{-2}. Figure 6c presents the elemental distribution within TiC particles at different aging temperatures. As the aging temperature increases, the concentration of C in the TiC particles shows a slight decrease, while the concentrations of Ti and W exhibit a moderate rise. This compositional evolution is attributed to the higher activation energies for diffusion of Ti and W compared to that of C at elevated temperatures.

Figure 6d presents the compositional distribution of the γ' precipitates, while Figure 6e illustrates the variation in the average content of major alloying elements within the γ' phase under different aging temperatures. As the aging temperature increases from 770 °C to 920 °C, the contents of Al and Ti in the γ' phase exhibit a slight increase, whereas those of Fe and Ni show a moderate decrease. This behavior can be attributed to the more pronounced enhancement in diffusion rates of Al and Ti atoms compared to Fe and Ni atoms at elevated aging temperatures, which influences the elemental partitioning behavior of the γ' phase [14].

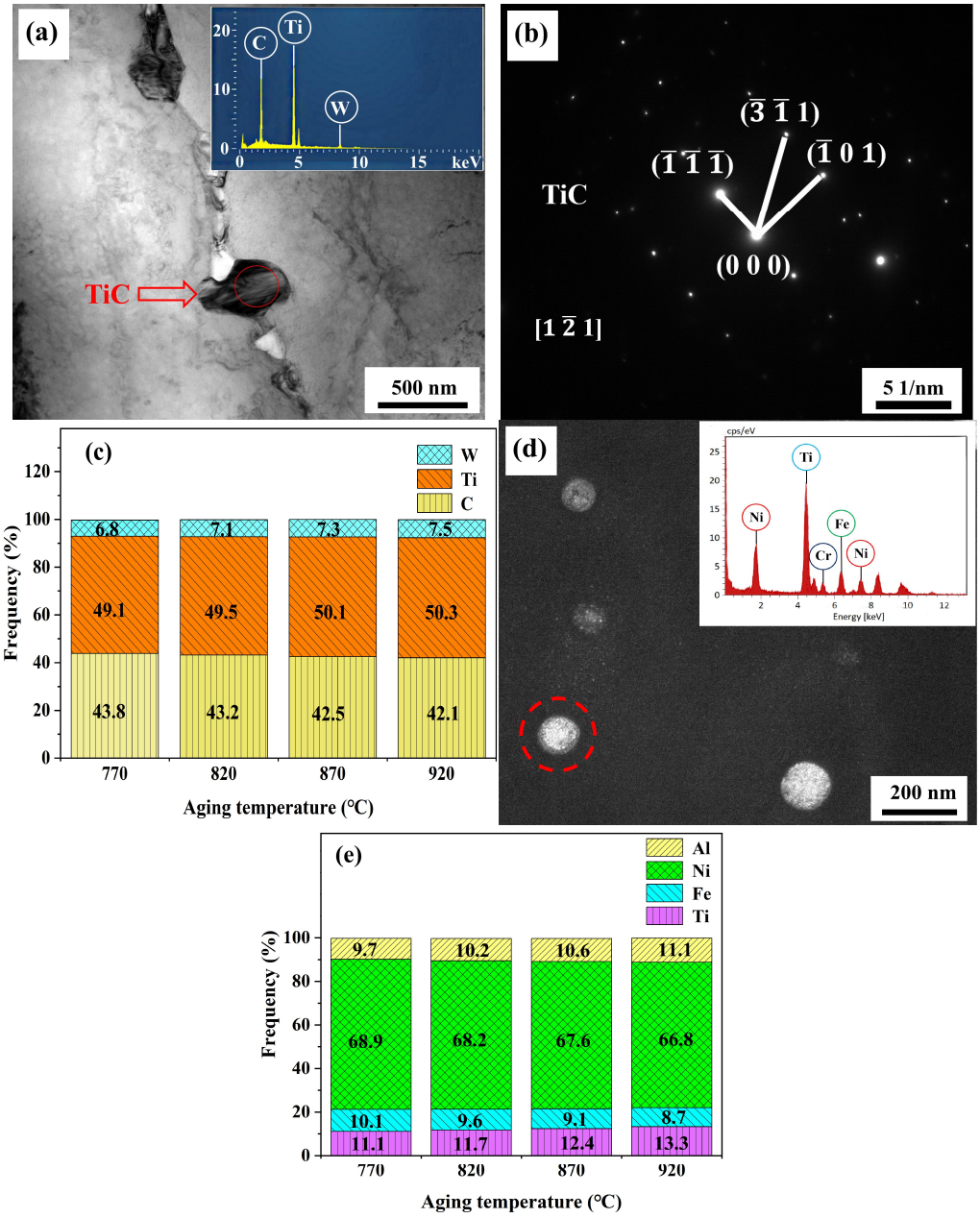


Figure 6. The microstructure of precipitates in the GH2787 alloys: (**a**) TEM micrograph; (**b**) the selected-area diffraction pattern of TiC particles; (**c**) The average element content in TiC particles; (**d**) the composition map of γ' particles; (**e**) The average element content in γ' particles after different aging temperature.

3.2.3. Interaction of Dislocations and Precipitates

Figure 7 displays the dislocation configurations in the GH2787 alloy subjected to different aging temperatures. Following the 1140 °C × 4 h solution treatment, transmission electron microscopy (TEM) observations revealed a relatively low dislocation density. These dislocations primarily originated from two sources: (1) dislocations pinned by undissolved second-phase particles during solution treatment, as well as those generated by localized plastic deformation due to thermal stresses before or after the solution process; and (2) dislocations introduced in the vicinity of precipitates during aging, resulting from localized plastic deformation induced by internal stress concentration associated with the formation of γ' particles [15,16]. After aging in the range of 820–920 °C, where the γ' precipitates were coarser, clear evidence of dislocation pinning by γ' particles

was observed. The results also demonstrate a notable decrease in dislocation density with increasing aging temperature. This trend is attributed to the enhanced thermal activation and accelerated atomic diffusion at higher aging temperatures (770–920 °C), which promote dislocation climb and annihilation processes, leading to a progressive reduction in dislocation density [17,18].

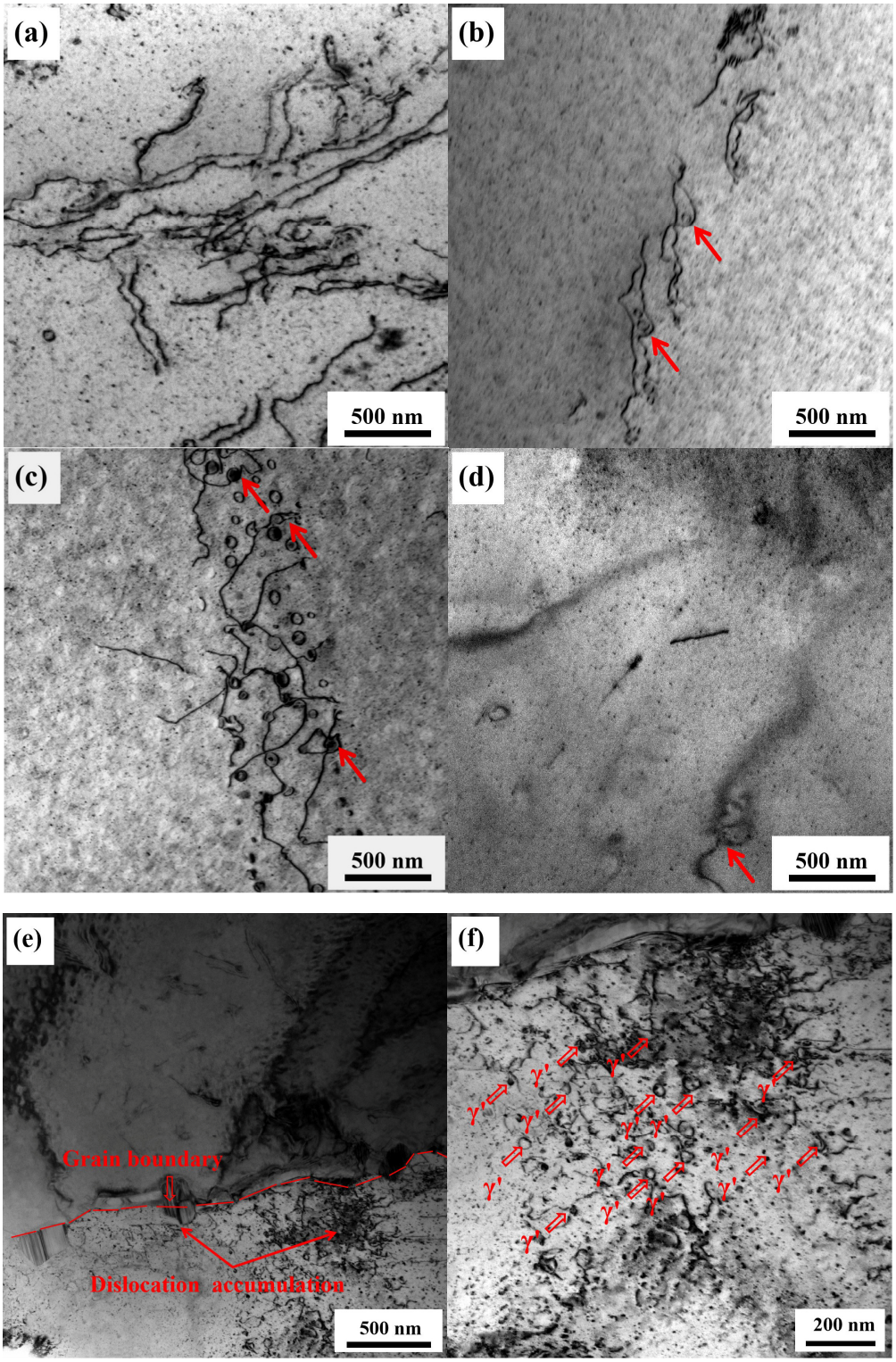


Figure 7. The dislocation morphology of the GH2787 alloys after different aging temperature: (**a**) 770 °C, (**b**) 820 °C, (**c**) 870 °C, (**d**) 920 °C, (**e**) Dislocations accumulate near the grain boundaries; (**f**) Dislocations accumulate in the regions enriched by γ′ particles.

Figure 7e,f clearly reveals the preferential accumulation of dislocations in two typical regions. As shown in Figure 6e, dislocations tend to accumulate markedly at grain boundaries. This phenomenon occurs because grain boundaries act as strong obstacles to dislocation motion. Under external stress, gliding dislocations continue to slip and converge in front of grain boundaries, where they are unable to transmit across, forming a configuration analogous to a "traffic jam"—a dislocation pile-up—that leads to significant dislocation aggregation near the interface [19]. Another typical dislocation configuration is shown in Figure 7f, where dislocations are effectively pinned in regions densely populated by γ' precipitates. The underlying mechanism is that these precipitates act as discrete obstacles that directly hinder dislocation glide on their slip planes [20]. To proceed, dislocations must either bypass the particles via the energetically costly Orowan bowing mechanism or shear through them by overcoming the interfacial energy barrier. When the resolved external stress is insufficient to activate either process, the dislocations remain stably pinned by the precipitates, resulting in the observed microstructure.

Figure 8a presents the XRD patterns of the GH2787 alloy subjected to different aging temperatures. Only the austenitic phase was detected in the patterns, confirming that the alloy matrix is predominantly austenitic. The diffraction angles and full width at half maximum (FWHM) of the diffraction peaks were measured using JADE 9.0 software, and the dislocation density under each aging condition was subsequently calculated [21,22], as summarized in Figure 8b. Dislocations influence the interplanar spacing (D) in GH2787 alloy, which in turn affects the diffraction angle of Bragg peaks in X-ray diffraction (XRD) patterns. By measuring shifts in diffraction angles and changes in the full width at half maximum (FWHM) of diffraction peaks, the dislocation density of the material can be quantitatively evaluated using a set of interrelated equations. According to the modified Williamson–Hall method [23]:

$$K = \frac{2\sin\theta}{\lambda} \tag{1}$$

$$\Delta K = \alpha + \beta K C^{1/2} \tag{2}$$

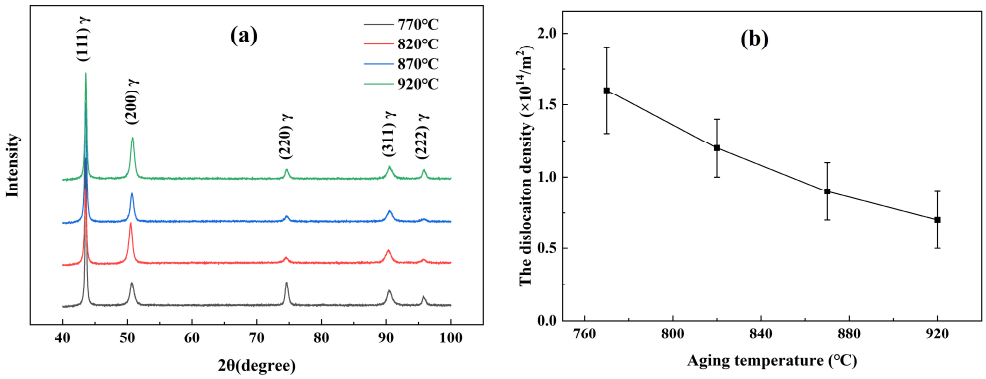


Figure 8. The XRD peaks and the calculated dislocation density of the GH2787 alloys after different aging temperature: (**a**) peaks density from 40° to 100°, (**b**) dislocation density.

Here, θ is the diffraction angle, λ is the X-ray wavelength, and ΔK represents the integral breadth of the diffraction peak. These parameters were obtained from XRD patterns processed with MDI Jade 6.5 software. C denotes the dislocation contrast factor, treated as a constant in Equation (2), and α is a size-related shape factor associated with the crystallite dimension.

For each specimen, XRD scans were performed over a 2θ range of 0–120°, yielding four distinct diffraction peaks. From each peak, values of ΔK and K (=2 sin θ/λ) were determined. A linear fit of ΔK versus K allows the coefficient α to be derived from the

intercept on the ΔK axis. With an appropriately chosen α and the corresponding Miller indices (*hkl*) of the diffraction peak, the dislocation density ρ can be calculated using the following expressions [24,25]:

$$\frac{(\Delta K - \alpha)^2}{K^2} = \beta^2 0.285(1 - qH^2) \tag{3}$$

$$H^2 = \frac{h^2k^2 + h^2l^2 + l^2h^2}{\left(h^2 + \mathrm{k}^2 + l^2\right)^2} \tag{4}$$

$$\rho = \frac{2\beta^2}{\pi \mathrm{b}^2 M^2} \tag{5}$$

In these equations, ΔK, α, and K retain the same definitions as in Equations (1) and (2). The parameter q is an experimentally determined constant, and H_2 is computed from the specific (*hkl*) reflection using Equation (4). The Burgers vector b is taken as 0.25 nm, and the Taylor factor M is set to 3. By performing a linear regression of ΔK versus K, the quantity $0.285\beta^2$ is obtained from the intercept on the ΔK axis, from which the dislocation density ρ is finally calculated via Equation (5).

With the increase in aging temperature from 770 °C to 920 °C, the dislocation density decreased markedly from $(1.6 \pm 0.3) \times 10^{14}$ m^{-2} to $(0.8 \pm 0.2) \times 10^{14}$ m^{-2}. These results demonstrate that high-temperature aging not only promotes the coarsening of precipitates but also effectively reduces the dislocation density in the alloy.

3.3. Fracture Morphology

Figure 9 presents the tensile fracture morphologies of specimens subjected to different aging temperatures. The fractographs reveal a mixed fracture mode consisting of both ductile fracture and cleavage fracture. The inset in the lower-left corner shows a 10× magnified view of the region marked by the central red circle. As the aging temperature increases from 770 °C to 920 °C, the proportion of the ductile fracture region is approximately 21%, 13%, 17%, and 29%, respectively. This variation correlates well with the trend observed in the post-elongation. Generally, dimples serve as microscopic evidence of significant plastic deformation prior to fracture. A larger area fraction of dimples indicates more extensive and sufficient plastic deformation during the fracture process, which macroscopically corresponds to a higher elongation. Quantitative statistical analysis was performed on at least 3000 dimples per sample to determine the average dimple size. With the aging temperature increasing from 770 °C to 920 °C, the average dimple sizes are 3.6 μm, 2.2 μm, 1.6 μm, and 1.9 μm, respectively. No direct correlation is found between the average dimple size and the post-elongation. The elongation of the GH2787 alloy is primarily governed by the area fraction of the ductile fracture region.

Figure 10 shows the impact fracture surfaces of the GH2787 alloy after aging at different temperatures. The fractographs reveal a mixed fracture mode, consisting of both intergranular brittle fracture and ductile dimple rupture. The insets in the lower-left corners of each image present magnified (10×) views of the dimple morphology. As the aging temperature increases from 770 °C to 920 °C, the area fraction of ductile fracture regions dominated by dimples varies in a fluctuating manner, measuring approximately 10%, 6%, 13%, and 16%, respectively. This variation aligns well with the trend observed in impact energy. The average dimple sizes, determined by measuring 2000 dimples per condition using the intercept method, are indicated in the upper-right corners of the images. The corresponding mean dimple diameters are 5.7 μm, 5.2 μm, 5.5 μm, and 6.1 μm for aging temperatures from 770 °C to 920 °C. In general, larger dimple sizes indicate extensive plastic deformation prior to fracture, where more energy is absorbed during the growth and

coalescence of microvoids, thereby resulting in higher impact toughness [26]. Conversely, smaller dimples reflect limited local plastic deformation capacity, leading to rapid void linkage and an increased tendency for brittle fracture, which correspondingly reduces impact toughness.

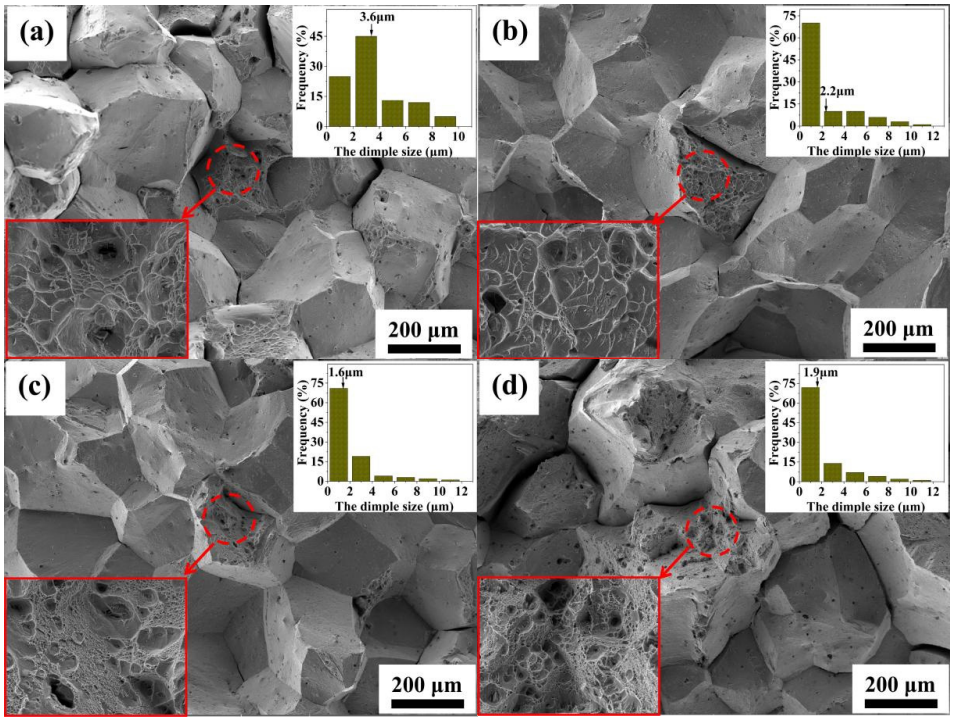


Figure 9. The fracture morphology of the stretched specimens at different aging temperatures: (**a**) 770 °C, (**b**) 820 °C, (**c**) 870 °C, (**d**) 920 °C.

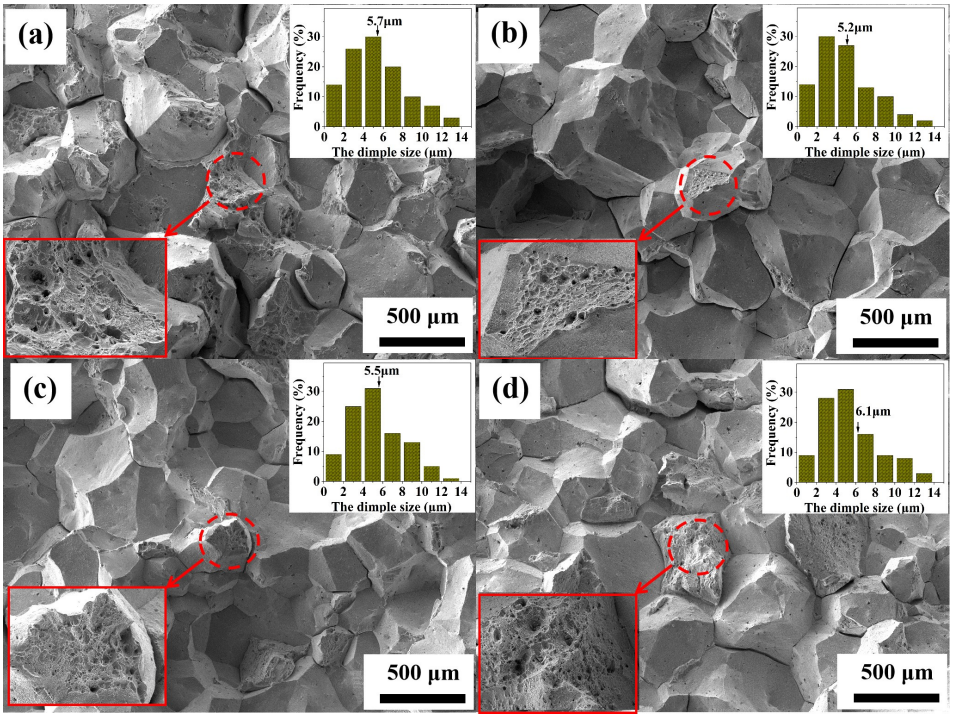


Figure 10. Impact fracture morphology at different aging temperatures: (**a**) 770 °C, (**b**) 820 °C, (**c**) 870 °C, (**d**) 920 °C.

4. Discussions

Based on the aforementioned results, it is evident that the aging temperature exerts a remarkable influence on both the mechanical properties and microstructural morphology of the GH2787 alloy. As the aging temperature increases from 770 °C to 920 °C, the tensile and yield strengths decrease rapidly (Figure 2a), accompanied by a significant coarsening and reduction in the number density of γ' precipitates (Figure 5a,b), as well as a notable decline in dislocation density (Figure 8b). These changes are primarily attributed to the accelerated diffusion of alloying elements at elevated aging temperatures, which drives the microstructural evolution of the γ' phase. As the main source of precipitation strengthening, the γ' precipitates also play a critical role in pinning dislocation motion. Thus, their morphology and volume fraction directly govern the mechanical response of the alloy. In general, the overall strength of the alloy is contributed collectively by lattice friction, solid solution strengthening, grain refinement strengthening, precipitation strengthening, and dislocation strengthening. To quantitatively elucidate the effect of aging temperature on these individual strengthening mechanisms, the overall yield strength can be decomposed as follows [27]:

$$\sigma_{\mathrm{y}} = \sigma_0 + \sigma_G + \sigma_{\mathrm{s}} + \sigma_P + \sigma_\rho \tag{6}$$

where σ_{y} is the yield strength, σ_0 is the internal friction stress of pure nickel, σ_G is the grain boundary strengthening, σ_{s} is the solid solution strengthening, σ_P is the precipitation strengthening, σ_ρ is the dislocation strengthening.

The lattice friction stress refers to the resistance encountered by a dislocation as it moves through the crystal lattice (denoted as τ_0). Its component along a specific normal stress direction can be resolved as:

$$\sigma_0 = \frac{\tau_0}{\cos\lambda \cos\varphi} = M\tau_0 \tag{7}$$

In this formulation, λ and φ represent the angles between the direction of the applied normal stress and the slip direction, and between the normal stress and the slip plane normal, respectively. The Schmid factor, defined as $M = 1/(\cos\lambda \cdot \cos\varphi)$, provides the geometric relationship for resolution. For instance, in pure nickel, where τ_0 is approximately 5.7 MPa and M is taken as 3.2, the corresponding σ_0 is thus derived as 18.2 MPa [28].

The strengthening effect arising from grain size is governed by the well-established Hall-Petch relationship, which quantifies the grain refinement strengthening:

$$\sigma_G = k\mathrm{d}^{-\frac{1}{2}} \tag{8}$$

where k is the Hall-Petch slope ($k \approx$ 500~700 MPa·μm$^{-(1/2)}$)and d is the effective grain size.

Roth Ref. [29] specifically investigated solid solution strengthening in nickel-based alloys and proposed the corresponding expression:

$$\sigma_{\mathrm{s}} = \left(\sum_i k_i^{1/n} c_i\right)^n \tag{9}$$

where c_i is the atomic concentration of the solute i element, and k_i is the strengthening constant of the solute i element.

The stress exponent "n" in solid solution strengthening models generally assumes a value between 1/2 and 1. It is well-established that for multi-component face-centered cubic (FCC) crystals, a value of *n* = 1/2 is most suitable [26]. Consequently, the atomic concentration of the solute elements in the GH2787 alloy, required for the calculation, is obtained by converting the mass fraction to an atomic fraction as follows:

$$\mathrm{wa}_i\ \% = (wt_i\% \div A_i) \div \sum_{i=1}^{N} (wt_i\% \div A_i) \tag{10}$$

where wt_i % is the mass concentration of element i in the alloy, and A_i is the atomic weight of element i. The relevant parameters in the calculation process are derived from Reference [30].

Precipitation strengthening in the GH2787 alloy is attributed predominantly to the γ' phase, while the contribution from the sparingly distributed TiC particles is negligible. Thus, the strengthening effect is evaluated with the following expression:

$$\sigma_P = \sigma_{P(\gamma')} + \sigma_{P(\mathrm{TiC})} \tag{11}$$

$$\sigma_{P(\gamma')} = 0.1MGb/\lambda_{i(\gamma')} \tag{12}$$

$$\sigma_{P(\mathrm{TiC})} = 0.1MGb/\lambda_{i(\mathrm{TiC})} \tag{13}$$

where M is the Taylor factor (=3.1), G is the shear modulus (80 GPa for GH2787 alloy), b is the length of the Burgers Vector (for a nickel-based alloy, b $\approx$ 0.5 nm), and λ_i is average particle spacing.

The strengthening contribution from dislocations can be calculated using the well-established Taylor relationship:

$$\sigma_\rho = \alpha MGb\sqrt{\rho} \tag{14}$$

where α is a constant (=0.5–1), G and b are shear modulus and Burgers Vector length, respectively. ρ is the dislocation density.

Figure 11 illustrates the calculated contributions of individual strengthening components to the overall yield strength of the material. Figure 11a shows the variation in strength components provided by different strengthening mechanisms as a function of aging temperature. It can be observed that the decrease in yield strength with increasing aging temperature from 770 °C to 920 °C is primarily attributed to a significant reduction in precipitation strengthening. Figure 11b further compares the experimentally measured and theoretically calculated yield strength values. The black curve represents the experimentally measured yield strength, which decreases from 715 ± 12 MPa to 433 ± 9 MPa as the aging temperature increases from 770 °C to 920 °C. The red curve denotes the yield strength calculated based on the superposition model of individual strengthening mechanisms, which declines from 738 ± 13 MPa to 408 ± 7 MPa over the same temperature range. The comparison reveals that the discrepancy between the calculated and experimental values is within 7%, indicating good agreement.

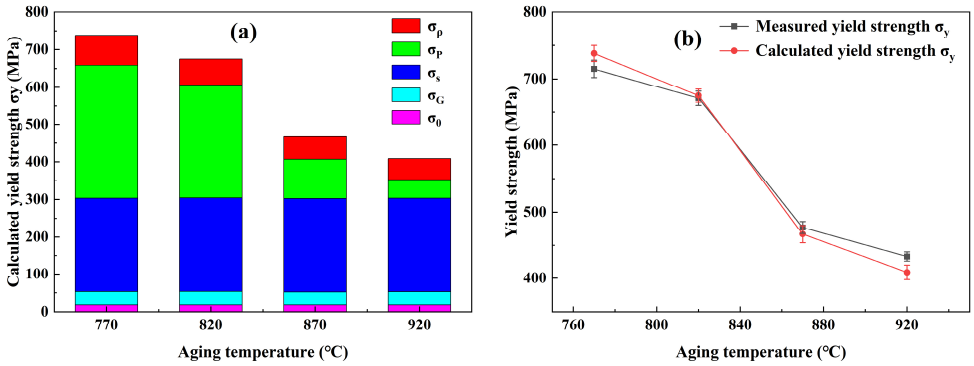


Figure 11. Yield Strength: (**a**) Calculation of each component of yield strength, (**b**) Comparison of calculated yield strength and tested yield strength.

5. Conclusions

This study systematically investigated the influence of aging temperature (770–920 °C) on the microstructure and mechanical properties of GH2787 alloy. The main conclusions are summarized as follows:

(1) After aging at 770 °C and 820 °C, the γ' precipitates are fine, densely dispersed, and exhibit small interparticle spacing. As the aging temperature increases to 870 °C and 920 °C, significant coarsening of the γ' particles occurs, accompanied by a sparser distribution and a notable increase in interparticle spacing. In addition, the dislocation density decreases significantly with increasing aging temperature.

(2) As the aging temperature increases from 770 °C to 820 °C, the ultimate tensile strength and yield strength show a moderate decrease. A more pronounced drop in both strength indicators is observed when the temperature is further raised to 870 °C and 920 °C. In contrast, the impact toughness follows a non-monotonic trend: it initially decreases, reaches a minimum at 820 °C, and then increases rapidly with further temperature increase up to 920 °C.

(3) Quantitative analysis of the strengthening contributions reveals that solid-solution strengthening and precipitation strengthening dominate the yield strength of the GH2787 alloy. The notable decrease in yield strength at elevated aging temperatures is primarily attributed to the reduction in precipitation strengthening. Additionally, differences in impact toughness can be linked to the quantity and dimensions of the dimples as revealed by fractographic analysis.

Author Contributions: Data curation and writing—original draft, Y.W.; Conceptualization and supervision, G.X.; Methodology and project administration, S.G.; Resources and supervision, S.L.; Supervision and funding acquisition, J.D.; Methodology and project administration, T.W.; Resources and supervision, Z.L.; Visualization and writing—review & editing, W.G. All authors have read and agreed to the published version of the manuscript.

Funding: This work was financially supported by the project "XX-2022-105" of the State Administration of Science, Technology and Industry for National Defense, and the project [XX-2022-100] of the State Administration of Science Technology and Industry for National Defense.

Data Availability Statement: The original contributions presented in this study are included in the article. Further inquiries can be directed to the corresponding authors.

Acknowledgments: We are grateful for the State Administration of Science, Technology, and Industry for National Defense's financial support.

Conflicts of Interest: Authors Yan Wang and Juan Deng were employed by the company AECC Chengdu Engine Co., Ltd., and Guohua Xu, Tianyi Wang, and Zhen Liu were employed by the company Gaona Aero Material Co., Ltd. The remaining authors declare that the research was conducted in the absence of any commercial or financial relationships that could be construed as a potential conflict of interest.

References

1. Sheng, M.; Sheng, R. High temperature creep properties of directionally solidified *CM*-247LC Ni-based superalloy. *Mater. Sci. Eng. A* **2016**, *655*, 237–243.
2. Li, J.; Yang, M. Particle size dependence of the microsegregation and microstructure in the atomized Ni-based superalloy powders: Theoretical and experimental study. *J. Mater. Sci. Technol.* **2024**, *171*, 54–65. [CrossRef]
3. Yang, Y.P.; Gao, Y.T. Synergistic evolution of MC/M23C6 carbides in a polycrystalline Ni-based superalloy during long-term aging: Elemental diffusion and interaction mechanisms. *Mater. Charact.* **2025**, *229*, 115462. [CrossRef]
4. Farias, F.W.C.; Duarte, V.R. High-performance Ni-based superalloy 718 fabricated via arc plasma directed energy deposition: Effect of post-deposition heat treatments on microstructure and mechanical properties. *Addit. Manuf.* **2024**, *88*, 104252.

5. Kumar, C.; Pavan, A.H.V. Role of threshold stress in creep of IN740H, a γ′-lean Ni-based superalloy. *Mater. Sci. Eng. A* **2024**, *903*, 146667. [CrossRef]
6. Mo, Z.; Xu, X. Effect of Diamond Rotary Rolling Treatment on Surface Property and Fatigue Life of GH2787 Superalloy. *Adv. Eng. Mater.* **2025**, *27*, 2402045. [CrossRef]
7. Zhou, Z.; Qi, L.; Zhang, L.; Cui, Z.; Shang, Y.; Qi, H.; Li, Y.; Jiang, L.; Nadimpalli, V.K.; Huang, L. Microstructural evolution of nickel-based single crystal superalloy fabricated by directed energy deposition during heat treatment. *J. Alloys Compd.* **2022**, *904*, 163943. [CrossRef]
8. Vattré, A.; Devincre, B.; Roos, A. Orientation dependence of plastic deformation in nickel-based single crystal superalloys: Discrete-continuous model simulations. *Acta Mater.* **2010**, *58*, 1938–1951. [CrossRef]
9. Zhang, H.; Ma, H.; Chang, T.; Zhang, Y.; Loge, R.E.; Zhang, Q.; Fang, X.; Huang, K. Deformation mechanisms of primary γ′ precipitates in nickel-based superalloy. *Scr. Mater.* **2023**, *224*, 115109. [CrossRef]
10. Zhao, C.; Liu, N.; Li, F.; Wu, G.; Li, F.; Yang, L. The influence of heat treatment procedures on the endurance properties and longitudinal low-microstructure of GH2787 alloy. *J. Iron Steel Res.* **2011**, *23*, 72–75. [CrossRef]
11. Li, X.; Chen, Y. Study on grain evolution law of GH2787 alloy blade forgings. *Hot Work. Technol.* **2022**, *51*, 22–26. [CrossRef]
12. Tang, S.; Ning, L.K.; Xin, T.Z.; Zheng, Z. Coarsening behavior of gamma prime precipitates in a nickel based single crystal superalloy. *J. Mater. Sci. Technol.* **2016**, *32*, 258–263. [CrossRef]
13. Chen, Y.; Babu, R.P.; Slater, T.; Mitchell, R.; Ciuca, O.; Preuss, M. On the diffusion-mediated cyclic coarsening and reversal coarsening in an advanced Ni-based superalloy. In *Phase Transformations in Multicomponent Melts*; Wiley-VCH Verlag GmbH & Co. KGaA: Weinheim, Germany, 2016; pp. 345–352.
14. Gong, X.F.; Yang, G.X.; Fu, Y.H.; Ming, C.; Xie, Y.Q.; Zhuang, J.; Ning, X.J. Solute diffusion in the γ′ phase of Ni based alloys. *Comput. Mater. Sci.* **2010**, *47*, 232–236. [CrossRef]
15. Zhu, Z.; Li, J.; Zheng, M.; Lu, Q.; Chen, W.; Wei, X.; Song, B. Atomic-scale insights into the frictional wear behaviour of nickel-based single-crystal high-temperature alloys in the γ/Laves phase. *Mol. Simul.* **2025**, *51*, 624–638.
16. Wang, C.; Umair, M.; Jiang, Y.; Nerella, D.K.; Ali, M.A.; Steinbach, I. Morphological evolution of γ′ and γ″ precipitation in a model superalloy: Insights from 3D phase-field simulations. *Comput. Mater. Sci.* **2025**, *256*, 113972. [CrossRef]
17. Yajima, M.; Yoshida, N.; Kajita, S.; Tokitani, M.; Baba, T.; Ohno, N. In situ observation of structural change of nanostructured tungsten during annealing. *J. Nucl. Mater.* **2014**, *449*, 9–14. [CrossRef]
18. Zhang, H.; Tong, Y.; Ji, X.X.; Huang, H.; Yang, L.; Hu, Y.; Zhang, X.; Hua, M.; Cao, S. Effect of Tantalum content on microstructure and mechanical properties of CoCrNiTax medium entropy alloys. *Mater. Sci. Eng. A* **2022**, *847*, 143322. [CrossRef]
19. Liu, W.; Cheng, Y.; Sui, H.; Fu, J.; Duan, H. Microstructure-based intergranular fatigue crack nucleation model: Dislocation transmission versus grain boundary cracking. *J. Mech. Phys. Solids* **2023**, *173*, 105233. [CrossRef]
20. Liu, J.Z.; Chen, J.H.; Yang, X.B.; Ren, S.; Wu, C.L.; Xu, H.Y.; Zou, J. Revisiting the precipitation sequence in Al-Zn-Mg-based alloys by high-resolution transmission electron microscopy. *Scr. Mater.* **2010**, *63*, 1061–1064.
21. Couchet, C.; Allain, S.Y.P.; Geandier, G.; Teixeira, J.; Gaudez, S.; Macchi, J.; Lamari, M.; Bonnet, F. Recovery of severely deformed ferrite studied by in situ high energy X-ray diffraction. *Mater. Charact.* **2021**, *179*, 111346. [CrossRef]
22. Liu, Z.; Huo, X.; Yu, Y.; Zhang, C.; Xiao, N.; Zhao, J.; Yang, Z. Influence of austenitizing temperature on the mechanical properties and microstructure of reduced activation ferritic/martensitic steel. *Mater. Sci. Eng. A* **2021**, *826*, 141934. [CrossRef]
23. Ungár, T.; Borbély, A. The effect of dislocation contrast on X-ray line broadening: A new approach to line profile analysis. *Appl. Phys. Lett.* **1996**, *69*, 3173. [CrossRef]
24. Takebayashi, S.; Kunieda, T. Comparison of the dislocation density in martensitic steels evaluated by some X-ray diffraction methods. *ISIJ Int.* **2010**, *50*, 875–882. [CrossRef]
25. Hajyakbary, F.; Sietsma, J.; Böttger, A.J. An improved X-ray diffraction analysis method to characterize dislocation density in lath martensitic structures. *Mater. Sci. Eng. A* **2015**, *639*, 208–218. [CrossRef]
26. Mohapatra, S.; Poojari, G.; Das, S.; Das, K. Insights into the dynamic impact behavior of intercritically annealed automotive-grade Fe–7Mn–4Al–0.18C steel. *Mater. Sci. Eng. A* **2023**, *887*, 145769. [CrossRef]
27. Reed, R.C. *The Superalloys Fundamentals and Applications*; Cambridge University Press: Cambridge, UK, 2006.
28. Yong, Q.L. *The Second Phase of Steel and Iron Material*; Metallurgical Industry Press: Beijing, China, 2006.
29. Roth, H.A.; Davis, C.L.; Thomson, R.C. Modeling solid solution strengthening in nickel alloys. *Metall. Mater. Trans. A* **1997**, *28*, 1329–1335. [CrossRef]
30. Gypen, L.A.; Deruyttere, A. Multi-component solid solution hardening. *J. Mater. Sci.* **1977**, *12*, 1028–1033. [CrossRef] [PubMed]

Disclaimer/Publisher's Note: The statements, opinions and data contained in all publications are solely those of the individual author(s) and contributor(s) and not of MDPI and/or the editor(s). MDPI and/or the editor(s) disclaim responsibility for any injury to people or property resulting from any ideas, methods, instructions or products referred to in the content.